Magnetic and structural properties of epitaxially grown FeTaN thin films

L. Varga, H. Jiang, T. J. Klemmer, and W. D. Doyle
Center for Materials for Information Technology, Department of Physics and Astronomy, University of Alabama, P.O. Box 870202, Tuscaloosa, Alabama 35487

E. A. Payzant
Diffraction and Thermophysical Properties Group, High Temperature Materials Laboratory, Oak Ridge National Laboratory, Oak Ridge, Tennessee 37831

(Received 10 October 1997; accepted for publication 26 February 1998)

Epitaxial FeTaN films (~1500 Å) were grown as a function of nitrogen flow rate on epitaxial Cu(001) buffer layers (~2000 Å) on Si(001) single crystal substrates to investigate the effect of Ta and nitrogen on the magnetocrystalline anisotropy and magnetostriction. Detailed structural investigation by transmission electron microscopy and x-ray diffraction showed that the FeTaN films were epitaxial with the Pitsch orientation relationship of FeTaN(110)‖Cu(001) and FeTaN⟨111⟩‖Cu⟨110⟩, which allows four different in-plane variants to coexist in the film. It was found that the saturation magnetization did not change with nitrogen addition (~1600 emu/cc) up to 2% lattice dilation. The values of K_1 and λ_{100} of Fe decreased slightly (20% and 10%, respectively), while λ_{111} increased with increasing nitrogen content and eventually changed sign at ~2% normalized lattice dilation. These results qualitatively agree with our earlier findings on (001) oriented FeTaN epitaxial films on MgO single crystal substrates. Also, our calculated saturation magnetostriction for nanocrystalline samples agrees very well with published data on the same FeTaN composition. Based on Hoffmann's ripple theory the ripple constant is calculated for nanocrystalline films using the Doyle–Finnegan model for the local average anisotropy and our measured single crystal constants. It was found that the effect of nitrogen on reducing the average anisotropy through the fundamental constants is not significant, and therefore the major factor in achieving a low ripple constant (i.e., soft magnetic properties) is the grain size, the number of grains across the thickness and the thin film stress. © *1998 American Institute of Physics.* [S0021-8979(98)01811-8]

I. INTRODUCTION

The ever increasing density of stored information in magnetic recording systems is the result of a continuous improvement in media and heads. Densities larger than 5 Gbits/in.[2] can be achieved only on high coercivity media ($H_C > 2000$ Oe), which will require inductive record heads with high saturation flux densities ($B_S > 10\,000$ G).[1] Until recently, $Ni_{81}Fe_{19}$ has been used as the pole material in most thin film inductive head applications, but its relatively low saturation flux density ($B_S \approx 10\,000$ G) limits the choice of media and therefore the recording density. One of the most promising candidates for replacing permalloy is the single phase FeTaN,[2,3] in which the saturation flux density is twice as large as $Ni_{81}Fe_{19}$ and 30% larger than $Ni_{45}Fe_{55}$.[4] There has been a great interest in this and other FeXN materials during the last few years, and much information has been accumulated on its nanocrystalline state. That work has focused mostly on the optimization of the soft magnetic properties, i.e., small coercivity, low magnetostriction, and high permeability.[3,5–8] However, the effect of nitrogen on the fundamental magnetic properties, the magnetocrystalline anisotropy, and magnetostriction, has not been studied experimentally. Cates and Alexander[9] gave theoretical predictions for λ_{100} and λ_{111} in FeTaN based on De Vries' earlier model[10] for interstitials in bulk Fe. Assuming that the magnetoelastic coupling constants depend on nitrogen content, and that there is a significant amount of intergranular phase in FeTaN films, Cates and Alexander could explain the observed linear increase of the saturation magnetostriction, λ_S, as a function of nitrogen concentration.

In this investigation we explored the fundamental physical properties of FeTaN and their role in determining the soft magnetic properties of the nanocrystalline films. The underlying theoretical model in our approach is Hoffmann's ripple theory[11–14] utilizing the Doyle–Finnegan[15] calculation of the local average anisotropy. Hoffmann's model predicts that soft magnetic properties can be improved by reducing grain size and the local anisotropy energy. The average local anisotropy energy is governed by a combination of magnetocrystalline and magnetoelastic energies, where the order of magnitude is determined by the fundamental magnetic properties: the magnetocrystalline anisotropy constant, K_1, and the magnetostriction constants, λ_{100} and λ_{111}. In order to determine the local average anisotropy of FeTaN, and therefore to understand the soft magnetic properties of nanocrystalline samples, a knowledge of K_1, λ_{100}, and λ_{111} is required. In this article we present experimental results on the structural and magnetic properties of epitaxially grown FeTaN films, and using these results the average local anisotropy of nanocrystalline films is calculated.

II. AVERAGE LOCAL ANISOTROPY

Since Hoffmann developed his analytical ripple theory[11] relating structural and magnetic properties, it is well known that the influence of the film structure on soft magnetic properties can be expressed by a single parameter, the so-called structure or ripple parameter, S, which is given by

$$S=\frac{K_S D}{\sqrt{n}}, \tag{1}$$

where K_S is the local average anisotropy, D is the mean diameter of the crystallites, and n represents the number of grains across the thickness. According to Hoffmann,[12,14] S reflects the effect of the nonideal structure on the soft magnetic properties, and for an ideal, homogeneous thin film S would be zero. The central parameter for nonideal films in this picture is K_S, which forces the magnetization to deflect locally from the mean direction of the magnetization (ripple). This local average anisotropy for randomly oriented nanocrystalline films including the effect of isotropic thin film stress, σ_i, was calculated by Doyle and Finnegan[15] by taking an appropriate average of the magnetocrystalline (assuming $K_2=0$) and magnetoelastic energies to be

$$K_S=\left(\frac{8}{105}\right)^{1/2}[\{K_1+\tfrac{3}{8}(\lambda_{100}-\lambda_{111})\sigma_i\}^2 + \tfrac{7}{16}\{\tfrac{3}{2}(\lambda_{100}-\lambda_{111})\sigma_i\}^2]^{1/2}. \tag{2}$$

Their model gave good agreement with the experimentally determined ripple parameter for plated permalloy wires, where S was obtained by measuring the transverse biased permeability.[13] Nanocrystalline FeTaN films are reported to have a $\langle 110\rangle$ fiber texture, which, following the methodology[16] of Doyle and Finnegan, leads to a value of K_S of

$$K_S^{\langle 110\rangle}=\left(\frac{1}{8\sqrt{2}}\right)[13\{K_1+\tfrac{12}{13}(\lambda_{100}-\lambda_{111})\sigma_i\}^2 + \tfrac{144}{13}\{\tfrac{3}{2}(\lambda_{100}-\lambda_{111})\sigma_i\}^2]^{1/2}. \tag{3}$$

Since the energy is isotropic in K_1 in the (111) plane of a cubic material, the smallest local average anisotropy energy is expected in this plane and K_S for a $\langle 111\rangle$ fiber texture is calculated to be

$$K_S^{\langle 111\rangle}=\frac{\sqrt{2\pi}}{3}[\{\tfrac{3}{2}(\lambda_{100}-\lambda_{111})\sigma_i\}^2]^{1/2}. \tag{4}$$

The comparison of the calculated average local anisotropy energies for the three different crystallographic textures as a function of isotropic thin film stress is shown in Fig. 1, assuming the values[17] for Fe of $K_1=4.8\times10^5$ erg/cc, $\lambda_{100}=+20.7\times10^{-6}$, and $\lambda_{111}=-21.2\times10^{-6}$. In order to properly understand the soft properties of FeTaN, it is clearly necessary to know K_1, λ_{100} and λ_{111}.

Another model for determining the local average anisotropy in Hoffmann's ripple theory for Fe based nitrides was introduced by Takahashi and Shimatsu,[18] in which they also assumed that K_1, λ_{100}, and λ_{111} were the same in FeXN as in Fe and that the contribution of the magnetoelastic energy to the average local anisotropy could be obtained from the tetragonal deformation caused by the nitrogen incorporation into the Fe lattice. Their model's basic assumptions were questioned,[16] since the observed value of λ_S in Fe based nanocrystalline nitrides is well known to be a linear function of nitrogen content,[7–9,19] which is not consistent with constant values of λ_{100} and λ_{111}. Also, the contribution of the isotropic thin film stress acting on each grain in the film cannot be ignored, and, above all, the equilibrium lattice constant of Fe–N is not an equivalent elastic strain of the Fe bcc lattice, as was assumed in their picture. Nevertheless, both models, assuming K_1, λ_{100}, and λ_{111} for Fe, gave good agreement with the experimentally determined value of S, but only because it was found to be dominated by the grain size and not the local anisotropy.[16]

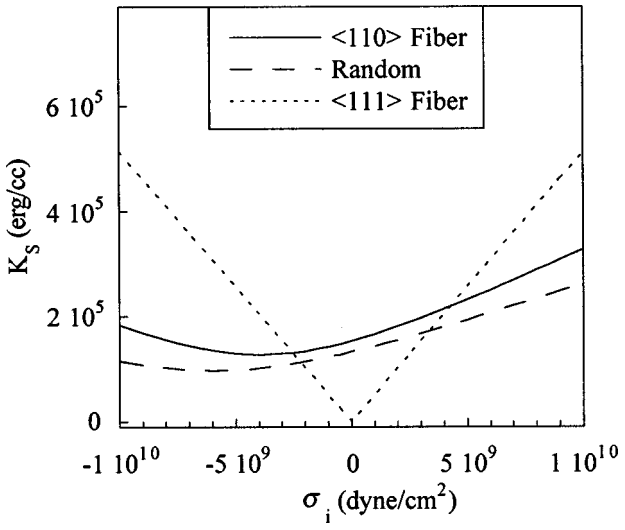

FIG. 1. Calculated local average anisotropy, K_S, for Fe as a function of isotropic thin film stress, σ_i, for different crystallographic textures.

III. EXPERIMENTAL METHOD AND RESULTS

Measurements of K_1, λ_{100}, and λ_{111} can be most accurately done on bulk single crystals, but the concentration of Ta and N in the FeTaN soft magnetic thin films[7,8] (1–5 at. % and 2–6 at. %) are well above their solubility limits in bulk Fe.[20] The magnetic measurements therefore were carried out on epitaxial thin films as deposited by dc magnetron sputtering (without annealing), which allowed the study of the same composition ranges used in nanocrystalline films with optimized soft magnetic properties.[3] The microstructure of the epitaxial films was thoroughly analyzed to support the interpretation of the magnetic measurements.

A. Epitaxial growth of FeTaN

The most suitable orientation for measuring crystalline anisotropy and magnetostriction constants in magnetic thin films of cubic materials is the (001) orientation, because in this plane the anisotropy energy contains only the fourth order magnetocrystalline anisotropy constant, and both λ_{100} and λ_{111} are easily accessible.[21] For a uniform stress the magnetoelastic energy does not have a contribution to the

anisotropy energy in this plane, if the two constant description is assumed.[22] In our initial work[23–25] we investigated (001) oriented FeTaN films on MgO single crystal substrates, and obtained information regarding K_1, λ_{100}, and λ_{111}. To obtain single phase epitaxial FeTaN films with nitrogen concentrations and growth orientation comparable to nanocrystalline films,[5,7,8] another substrate material, promoting the growth of (110) orientation, was chosen for the current work. The results of the (001) oriented films will be summarized and compared to these films in Sec. IV.

The lattice parameters of FeTaN are relatively close to Fe. Consequently any single crystal substrate material which promotes the epitaxial growth of Fe is a good candidate for FeTaN growth as well. The misfit for Fe[111] on Cu[110] is approximately 3%. Therefore, according to the invariant line criterion,[26] Fe with (110) orientation can be epitaxially grown[27] on Cu(001) single crystal with the Pitsch orientation relationship of Fe⟨111⟩‖Cu⟨110⟩. It has also been shown that Cu with an (001) orientation epitaxially grows on hydrogen terminated Si(001) single crystal substrates with an in-plane orientation of Cu⟨100⟩‖Si⟨110⟩.[28,29] This suggested the possibility of depositing a Cu buffer layer *in situ* before the FeTaN deposition, providing a clean, fresh surface, which is essential for epitaxial growth.

Si(001) substrates were dipped into diluted (10%) HF solution for 1 min to form an H-terminated surface[30] and then mounted into the vacuum chamber immediately. The base pressure was $2-3\times10^{-7}$ Torr after ~10 h pump down time. The purity of the 2 in. diameter Cu and Fe targets used in the dc magnetron sputtering sources was 99.9% by weight. The FeTa target was found to contain carbon contamination which gave traces of C in the FeTaN films as shown by Auger and x-ray photoelectron spectroscopy (XPS) analysis. Since the role and effect of nitrogen and carbon in the bcc Fe lattice is indistinguishable, and all the properties of FeTaN films were measured as a function of lattice dilation with nitrogen addition, the effect of carbon will be taken up by the lattice dilation of the FeTa films prepared at zero nitrogen flow. The lattice parameter of bulk[31] FeTa with 10 wt% Ta is 2.885 Å, and in our case it was 2.898 Å. The copper deposition was done at an argon pressure of 0.4 mTorr at a fixed sputtering power of 100 W, which gave a growth rate of ~8.8 Å/s. Immediately after the deposition of the ~2000 Å thick Cu buffer layer, the magnetic films were grown in a total argon–nitrogen pressure of 0.4 mTorr at a fixed total Ar–N_2 gas flow rate of 12 sccm and sputtering power of 35 W. The nitrogen content of the FeTaN films was varied by controlling the ratio of the Ar–N_2 flow rates during deposition. The growth rate for the ~1500 Å thick magnetic films was 1.2 Å/s. All depositions were carried out at ambient temperature. The sputtering pressure and power for the deposition of the magnetic layers were chosen to obtain the slowest possible growth rate while maintaining a stable magnetron plasma.

B. Structural characterization

X-ray diffraction analysis and conventional transmission electron microscopy (TEM) were used to obtain a thorough understanding of the films' structural characteristics. Standard x-ray diffraction analysis was performed using a two circle Rigaku D/Max-2BX diffractometer with Cu $K\alpha$ radiation and the pole figure measurements were carried out on a Scintag four circle diffractometer with Cr and Cu $K\alpha$ radiations using 5° steps in both rotation ($\Phi=0-360°$) and tilt ($\psi=0-70°$). A Hitachi H-8000 TEM operating at 200 kV was used for the electron microscopy.

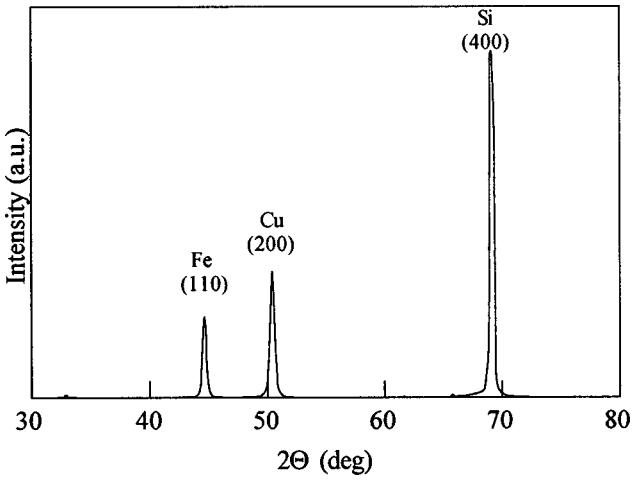

FIG. 2. High angle x-ray spectrum of epitaxial Fe(110) on Cu(001)/Si(001).

A standard high angle x-ray diffraction spectrum of the Fe/Cu/Si sample is shown in Fig. 2. According to the Bragg–Brentano x-ray geometry, the observed peaks correspond to the allowed reflections of crystallographic planes parallel to the sample surface. Therefore it can be concluded that Fe(110)‖Cu(001)‖Si(001).

It is well known that in sputtered thin films of FeTaN the tantalum and nitrogen form a solid solution with Fe,[5,7,8] where the Ta acts substitutionally and the N occupies the octahedral interstitial positions. The atomic radius of Ta is 16% larger than that of Fe, and hence it is above the Hume–Rothery size limit (15%) allowed for substitutional solid solutions.[32] The N atom is approximately three times larger than the octahedral site in the Fe lattice, and consequently a tetragonal distortion of the bcc Fe unit cell is expected with nitrogen incorporation, although the predicted tetragonality is relatively small ($c/a<1.10$).[33] As the nitrogen concentration increased, there was no evidence from x-ray diffraction of the formation of nitrides (e.g., TaN, γ-$(FeTa)_4N$, etc.) or other phases. The effect of Ta and N on the Fe(110) diffraction peak is shown in Fig. 3. It is observed that the peak decreases in intensity, broadens and shifts to larger d values (smaller 2θ) with Ta and nitrogen addition. The broadening of the Fe(110) peak can be the result of two different contributions: (a) the nonuniform microstress caused by the relatively large Ta atoms and the interstitial nitrogen atoms in the Fe lattice; and (2) a refinement of the grain size. The shift of the peak is the result of an average expansion of the lattice constant caused by these microstrains. The shifts and broadening are characteristics of increasing nitrogen content in FeTaN thin films[7] and in this study the shift of the (110) peak normalized to Fe, Δd_{110}, will be used to quantify the amount of incorporated interstitials in the FeTaN films

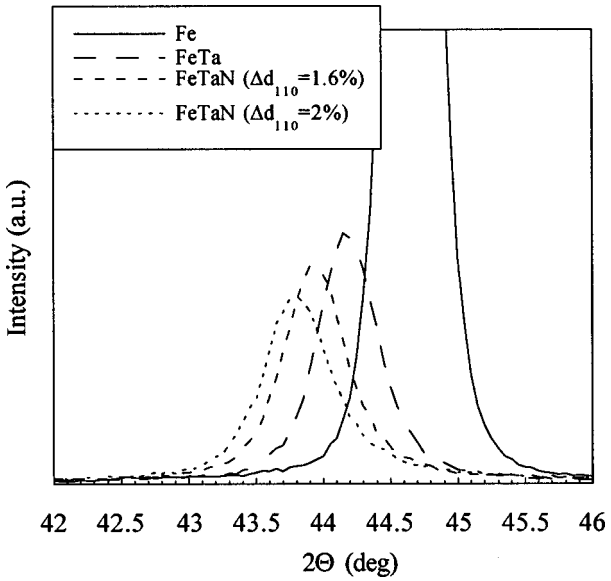

FIG. 3. The (110) peaks of Fe, FeTa, and FeTaN epitaxial films from the high angle x-ray spectra.

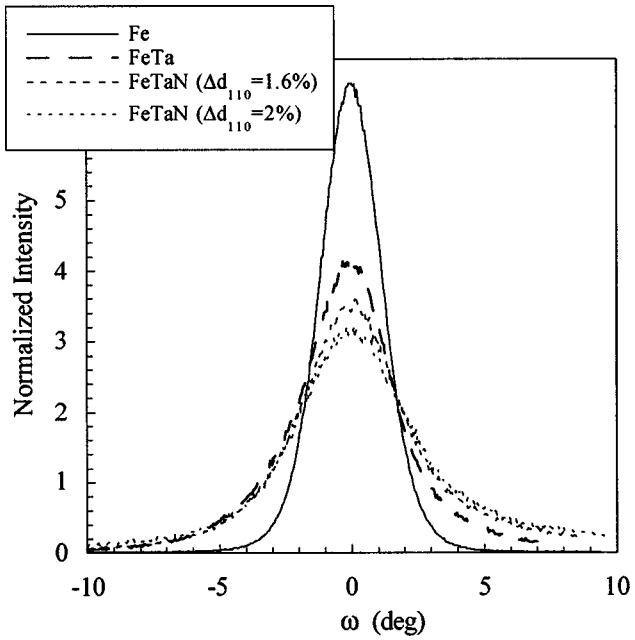

FIG. 4. Comparison of normalized rocking curves of (110) planes of Fe, FeTa, and FeTaN epitaxial films.

$$\Delta d_{110}(\%) = \frac{d_{110}^{\text{film}} - d_{110}^{\text{Fe}}}{d_{110}^{\text{Fe}}} \times 100. \tag{5}$$

The accuracy of the d-spacing measurement is higher than the accuracy of other available techniques XPS and Auger spectroscopy) for direct measurement of the nitrogen concentration, although the obtained atomic concentration of nitrogen depends on the unit cell volume, where the cell can be taken as body-centered-tetragonal (bct) or bcc,[7] and the presumed position of the nitrogen atoms. It also neglects thin film stress effects. Our calculated atomic concentration of nitrogen for a film with 2% lattice dilation was ~2 at. %—assuming bct deformation with the c axis out of the sample plane—which was the same order as determined by Auger spectroscopy (3±2 at. %). Since one of our goals is to compare calculated properties from measured single crystal constants with published experimental properties of nanocrystalline samples, the most reliable variable for the sake of comparison is the measured lattice dilation, which does not depend on the interpretation of the unit cell expansion.

Rocking curves were measured on the (110) peaks as a function of lattice dilation caused by the nitrogen incorporation, and are shown in Fig. 4. The intensities were normalized to the average intensity for each sample and ω is defined as the angle between the normals of the sample plane and the detected (110) planes. The full width at half maximum (FWHM) of the rocking curves can be used to describe the tilt of the (110) planes relative to the sample surface and therefore provides a quantitative comparison between the Fe based thin films. It is observed that the FWHM is 2.7° for pure Fe and increases to 3.9°, 4.3°, and 4.8° for the FeTa, FeTaN (Δd_{110}=1.6%, Δd_{110}=2%), respectively. In addition to the strains produced in the Fe lattice, it can be expected that small rotations of the crystallographic planes would be produced in the vicinity of the solute atoms resulting in a larger skew of the (110).

The structural results presented so far are not unique to epitaxial films, but could also be attributed to a strong ⟨110⟩ fiber texture. To understand the orientation relationship or epitaxy between the substrate and films, pole figure analysis was utilized. A (220) pole figure for the Cu buffer layer is shown in Fig. 5 with the horizontal and vertical lines being parallel to the Si⟨100⟩ directions. The Cu(220) pole intensities are positioned at 45° tilt and at 45° to the vertical and horizontal lines which corresponds to the orientation relationship of Cu(001)‖Si(001) with Cu⟨010⟩‖Si⟨110⟩. There was no sign of secondary orientations in the Cu buffer layer, and the high pole intensities suggest high quality epitaxial films.

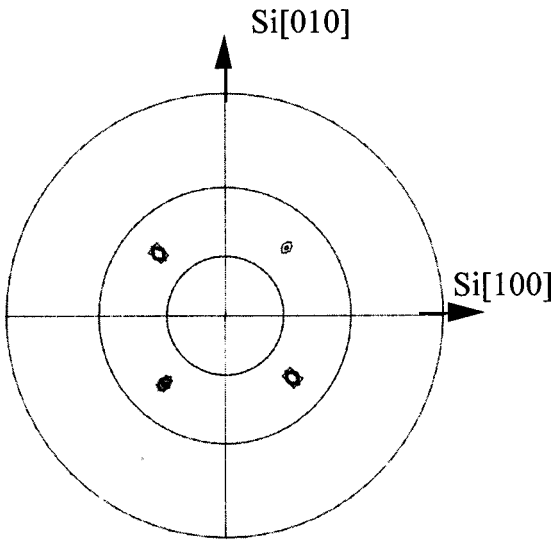

FIG. 5. The (220) pole figure of the 2000 Å epitaxial Cu(001) buffer layer on Si(001). The vertical and horizontal lines are parallel to Si⟨100⟩.

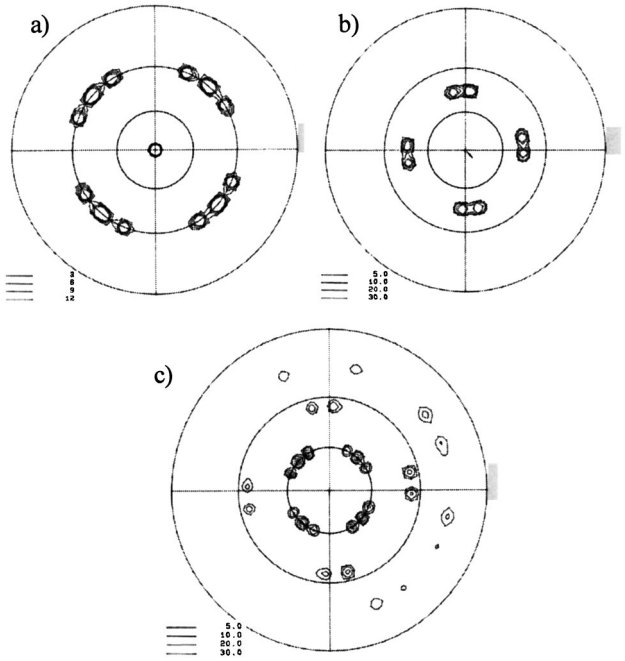

FIG. 6. The (a) (110), (b) (200), and (c) (211) pole figures of Fe epitaxial film on Cu(001)/Si(001.

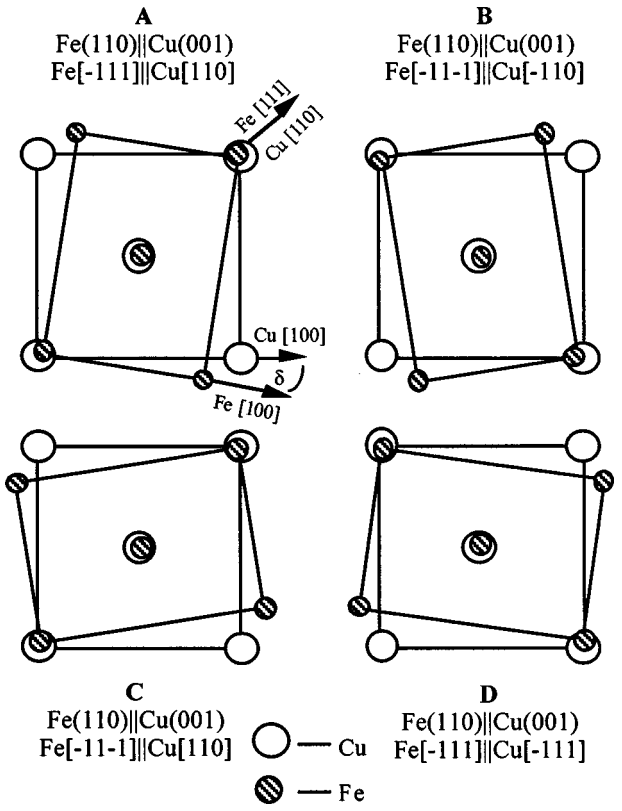

FIG. 7. The atomic configurations consistent with the Pitsch orientation relationship between Fe and Cu, where A, B, C, and D denote the four possible in-plane orientations. The angle between Cu⟨010⟩ and Fe⟨110⟩ is $\delta=9.7°$.

The (110), (200), and (112) pole figures of the pure Fe film are shown in Figs. 6(a)–(c), and they are positioned with the vertical line parallel to Cu$[\bar{1}10]$ and the horizontal parallel to Cu[110]. All the intensities can be indexed assuming four different in-plane variants of the orientation relationship of Fe(110)‖Cu(001) with Fe⟨111⟩‖Cu⟨110⟩ which corresponds to the Pitsch relationship.[26] The atomic configuration of these variants which coexist on the Cu buffer layer is shown in Fig. 7 with A, B, C, and D depicting these different orientations. A (110) Φ scan (rotation) at 60° tilt for the pure Fe sample is shown in Fig. 8 to demonstrate the contributions of the four variants on the pole figure. The labels indicate the A, B, C, and D orientations contributing to the intensity of the peaks. Similarly, the intensities in the other Fe pole figures correspond to these four inplane variants. The distinctly resolved peaks of the in-plane variants (Fig. 8) evidences a narrow in-plane, rotational spreading within the pure Fe film, estimated from the FWHM of the peaks to be ~6°.

A comparison of the (110) pole figures for different nitrogen content films is shown in Figs. 9(a)–9(d). Because the d_{110} of nitrided FeTa and the d_{111} of Cu are very close to each other, the strong Cu peaks which appeared at ~55° tilt were subtracted from the pole figures. This was justified experimentally by showing that at 50° and 60° tilt the Cu(111) was completely absent. Compared to the Fe, the FeTa and the FeTaN films have a broader in-plane distribution of the four variants by a few degrees. To demonstrate this, the intensities of the (110) pole figures at 60° tilt were replotted as a line scan for Fe, FeTa, and FeTaN samples and are shown in Fig. 10. There is a clear increase in the in-plane spread of the four variants for the FeTa films compared to the pure Fe; however, there is little increase in spreading as the nitrogen content increases. The spread was estimated for FeTa using a Φ scan with a smaller step size to have a FWHM of ~14°. It would be expected that if the strains associated with the solute atoms were distributed equally throughout the lattice, the lattice expansion would result in a better match, i.e., more perfect epitaxy of the FeTaN films on Cu. However, these distortions are localized in the vicinity of the solute atoms which tend to break up the perfection of the Fe lattice causing a larger distribution of the planes. The high nitrogen content films were found to also have a few percent volume fraction of a secondary orientation characterized by (110)

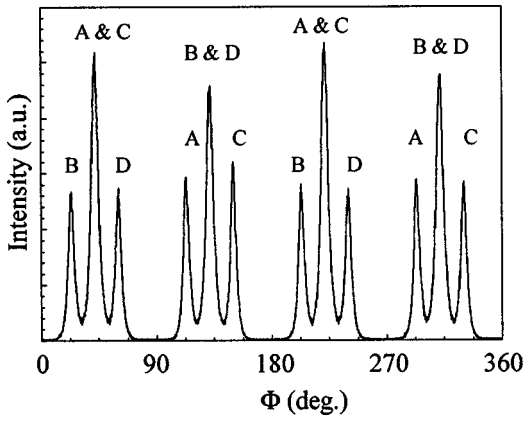

FIG. 8. Φ scan of Fe(110) at $\Psi=60°$ tilt. The A, B, C, and D represent the four in-plane variants contributing to the intensities of the peaks (high resolution).

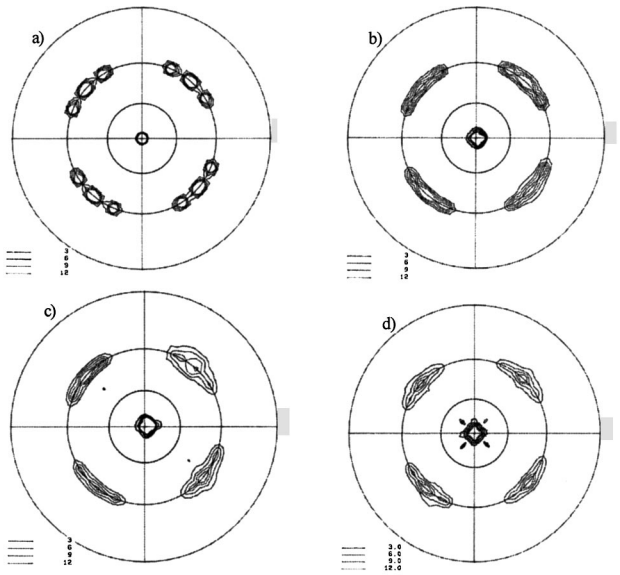

FIG. 9. Comparison of the (110) pole figures for (a) Fe, (b) FeTa, and (c–d) FeTaN epitaxial films.

intensities located at 45° away from the vertical and horizontal lines and tilts ~15° and 50°. These poles, together, can be indexed as resulting from an orientation relationship near FeTaN(123)‖Cu(001) with FeTaN⟨111⟩‖Cu⟨110⟩.

The pole figures were measured only up to 70° because of instrumental limitations. A way to get information at the 90° position and to confirm the results of the pole figure analysis is by using in-plane TEM selected area diffraction (SAD). The SAD for the pure Fe film is shown in Fig. 11(a) with a diagram, illustrated in Fig. 11(b), indexing the reflections from the four different variants. The relative positions

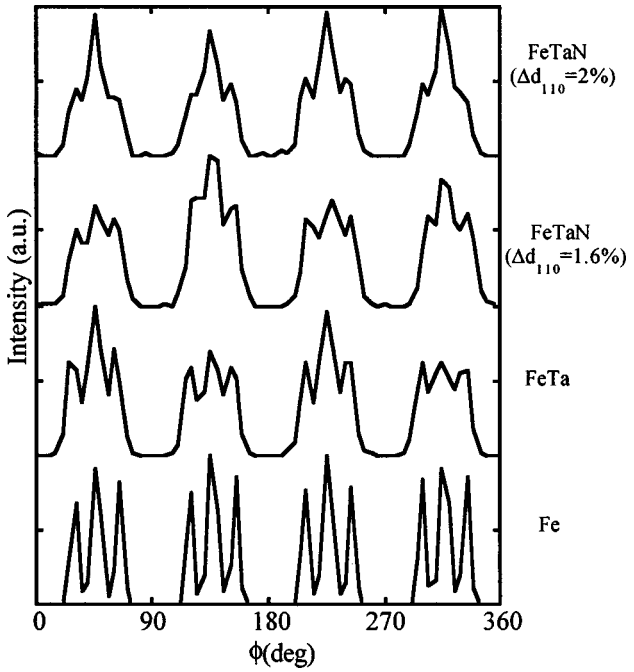

FIG. 10. Comparison of (110) Φ scans of Fe, FeTa, and FeTaN films (low resolution).

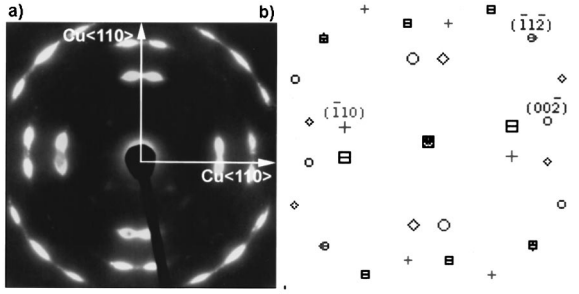

FIG. 11. Selected area diffraction pattern of the (110) oriented epitaxial Fe film on Cu(001)/Si(001). The pattern can be indexed assuming the A (marker ⊟), B (+), C (◇), and D (○) in-plane variants of the (110) orientation (see Fig. 7).

of the (110) reflections provide information at the 90° tilt of the (110) pole figure. The same is true with the (200) and (112) reflections completing the (200) and (112) pole figures. A comparison of the SAD patterns for the Fe based films is shown in Fig. 12 which confirms the presence of the four in-plane variants and the increase of the in-plane spread with the incorporation of Ta. There was no indication of nitrides (e.g., TaN, γ-$(FeTa)_4N$, etc.) or other phases on the SAD patterns, confirming the x-ray diffraction data, which is a less reliable phase identification method in the pole figure geometry. The films with high nitrogen content were found to contain (301) and (123) reflections in the SAD pattern (marked in the figure) which were not observed in the Fe and FeTa samples. These reflections are not expected in a ⟨110⟩ zone axis. However, they are in positions that coincide with the projection of the (301) and (123) poles which normally could be at 77° and 79° to the sample normal, respectively. The intensity distribution of these reflections cannot be the result of a well defined orientation near FeTaN(123)‖Cu(001)

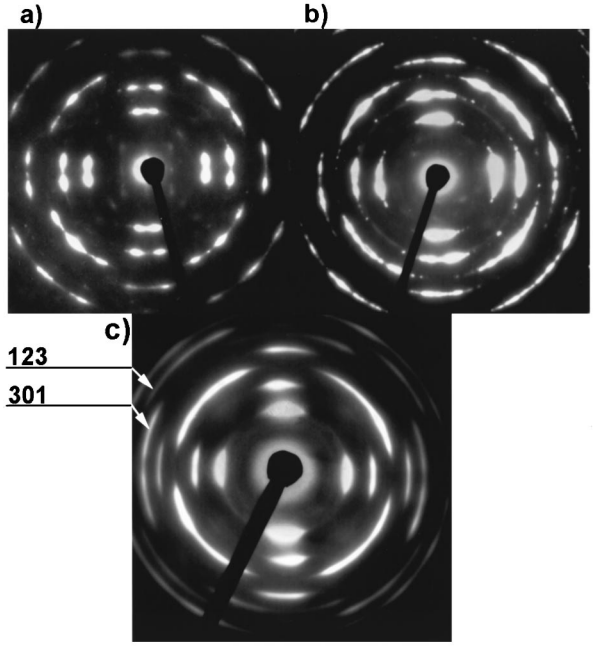

FIG. 12. Comparison of SAD patterns of (a) Fe, (b) FeTa, and (c) FeTaN epitaxial films.

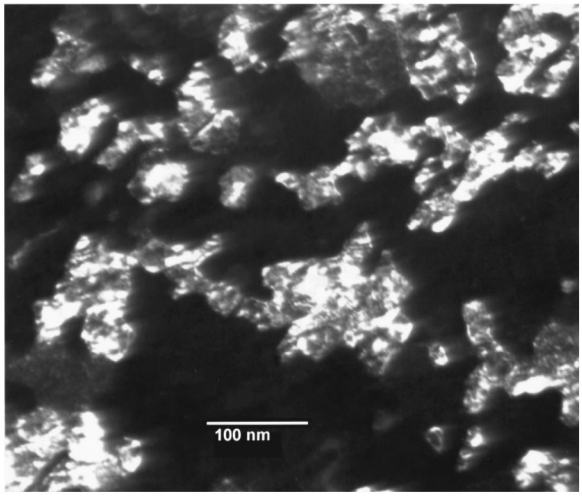

FIG. 13. Dark field image of FeTa sample in planar view.

with FeTaN$\langle 11\bar{1}\rangle \| \mathrm{Cu}\langle 110\rangle$ which was observed in the pole figure analysis, although this orientation does fall into the distribution. It can be concluded that, in the high nitrogen films, the diffraction conditions of the four variants are relaxed as the result of the increased slant of the (110) parallel to the surface and the increased strain of the lattice.[34]

The epitaxial growth of the (110) Fe based films on the (001) Cu results in a microstructure consisting of a mosaic of the four variants. The typical in-plane structure observed by dark field (DF) TEM utilizing the (110) reflections of two variants which are ~20° away from each other is shown in Fig. 13. The observed complex shapes of the different variants makes the grain size determination difficult and misleading. However, the features of the mosaic microstructure are on the order of ~1000 Å. The evolution of this type of microstructure is discussed in detail by Dahmen and Westmacott[35] for a bicrystal of (110) Al on (001) Si, and can be easily developed for a quadcrystal arrangement.

There is some speculation about the nature of the grain boundaries in the nanocrystalline FeTaN and its role in the soft magnetic properties.[3] The grain boundaries produced as a result of the epitaxial growth of the four variants are simplified versions of what would be found in randomly and especially $\langle 110\rangle$ fiber oriented nanocrystalline films. This is an added benefit of the (110) oriented films over the (001) films studied previously.[23,24] Because of the nature of the deposition, most of the grain boundaries are nearly perpendicular to the substrate surface resulting in boundaries of mostly tilt character. From the SAD analysis it can also be concluded that the misorientations across the boundaries can be classified as 20°, 90°, and 110° $\langle 110\rangle$ tilt boundaries. These boundaries in coincidence site lattice notation are close to $\Sigma = 33_a$, 17_b and 3, respectively.[36] It should be pointed out that the $\Sigma = 3$ misorientation is the well known twin in cubic materials and is expected to be of low energy when on specific crystallographic planes (e.g., (112) in bcc).[37] However, there is no clear faceting of the boundaries in these films, which is mainly the result of the nonequilibrium nature of the sputtering conditions. Annealing should cause a rearrangement of the boundary habit planes into stable positions. A detailed investigation of the exact nature of these boundaries would require high resolution TEM and is beyond the scope of the current study.

C. Magnetic characterization

The saturation magnetization and the magnetocrystalline anisotropy of the samples were measured on 6 mm diam disks using a vibrating sample magnetometer and a torque magnetometer. The samples were masked with wax, dipped into diluted HF (1:9) solution for few seconds to remove the FeTaN, taking advantage of the negligible etching rate of Cu on this time scale. Then the thickness of the formed steps on the copper buffer layer were measured with a Dektak Profilometer, and the volumes calculated from the sample area.

The magnetic properties of the mosaic structure can be calculated, based on the structural analysis, by taking the four in-plane variants into account and calculating the average properties. The anisotropy energy is obtained by summing the crystalline anisotropy energy and the magnetoelastic energies

$$\begin{aligned} E = {} & K_1(\alpha_1^2\alpha_2^2 + \alpha_1^2\alpha_3^2 + \alpha_2^2\alpha_3^2) + K_2(\alpha_1^2\alpha_2^2\alpha_3^2) \\ & - \tfrac{3}{2}\lambda_{100}\sigma(\alpha_1^2\gamma_1^2 + \alpha_2^2\gamma_2^2 + \alpha_3^2\gamma_3^2) - 3\lambda_{111} \\ & \times \sigma(\alpha_1\alpha_2\gamma_1\gamma_2 + \alpha_1\alpha_3\gamma_1\gamma_3 + \alpha_2\alpha_3\gamma_2\gamma_3), \end{aligned} \tag{6}$$

where K_1 and K_2 are the fourth and sixth order crystalline anisotropy constants, λ_{100} and λ_{111} are the magnetostriction constants. The α_i and γ_i are the direction cosines of the magnetization and the thin film stress, σ, in the materials coordinate system. Substituting the proper direction cosines for the four in-plane variants into Eq. (6), the angle dependent part of the energy is calculated to be

$$E = \left(\frac{3K_1}{16} + \frac{K_2}{32}\right)\sin^2 2\theta \cos 4\delta, \tag{7}$$

where θ is the angle of the magnetization measured from the Si[110] in the sample plane, and $\delta = 9.7°$, defined by the Pitsch orientation relationship (Fig. 7). E is a biaxial energy, which gives easy axes parallel to the $\langle 110\rangle$ directions of the Si substrate.

The hysteresis loops as a function of orientation in the sample plane (Fig. 14) and the fourfold symmetry of the torque curves (Fig. 15) confirmed the calculated biaxial symmetry. The symmetry is also in agreement with ferromagnetic resonance studies on Fe/Cu/Si by Naik *et al.*[38]

The expected torque per unit volume, calculated from Eq. (7) is

$$L = -\left(\frac{3K_1}{8} + \frac{K_2}{16}\right)\sin 4\theta \cos 4\delta. \tag{8}$$

The torque contributions from each of the four orientations and their sum are shown in Fig. 16. The 2θ and 6θ parts of the torque curves in the (110) planes are canceled due to the fourfold symmetry of the in-plane structure. The value of K_1 was extracted from the experimental torque data by fitting it with Eq. (8), assuming that K_2 is negligible compared to K_1 (Fig. 15). The value of the magnetocrystalline anisotropy constant, K_1, and the saturation magnetization, M_S, as a

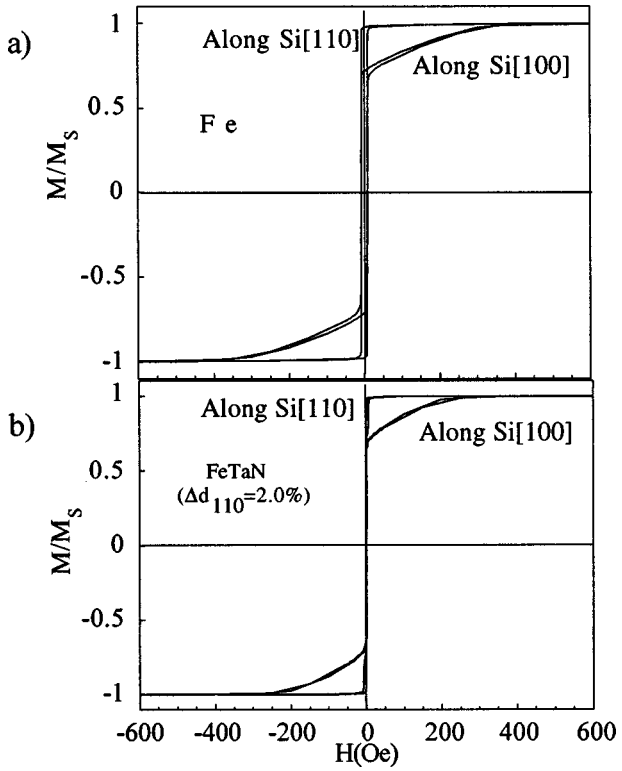

FIG. 14. Hysteresis loops along the easy and hard directions for Fe and FeTaN films.

function of normalized lattice dilation are plotted in Fig. 17. The K_1 and M_S determined for the pure Fe film agrees with the bulk values within the experimental error. The fact that the value of K_1 for Fe films agreed with bulk values supports the assumption that the anisotropy can be averaged over the four orientations. The saturation magnetization, which does not change significantly with nitrogen addition, is ~1600 emu/cc which agrees with published values of M_S for this composition.[5,6,23] The value of K_1 decreases with increasing nitrogen content, and at 2% lattice dilation is ~20% smaller than the value for pure Fe.

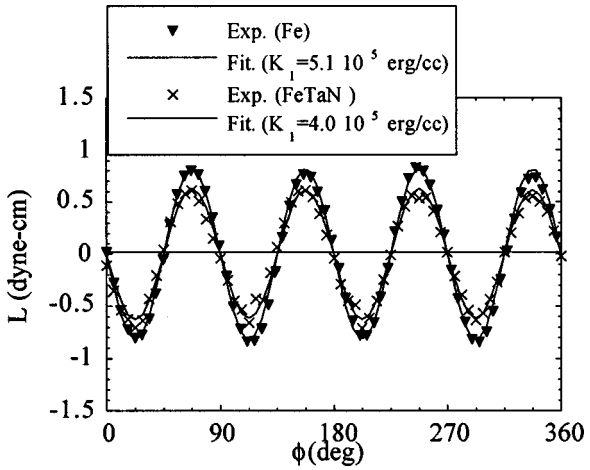

FIG. 15. Measured and calculated torque curves for Fe and FeTaN epitaxial films.

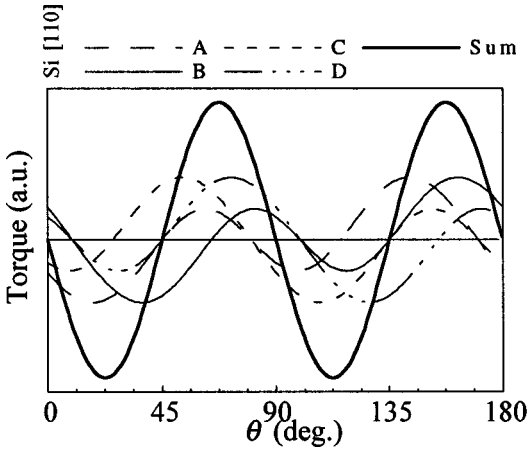

FIG. 16. Calculated torque contributions of the four in-plane variants and their sum.

The measurement of the saturation magnetostriction constants was carried out on a cantilever system,[39] which measures the substrate bending under the anisotropic thin film stress of the magnetostrictive thin film, using a field of 1 kOe rotating at a frequency of 10 Hz in the sample plane. This field was sufficient to saturate the samples which had a maximum anisotropy field of ~500 Oe. The interpretation of the substrate deflection in this mosaic structure is somewhat complicated.[40] Because of the peculiar combination of the four in-plane orientations, there is no direction in the sample plane which would only contain the [100] or [111] directions. In order to accurately obtain λ_{100} and λ_{111}, the magnetostriction was measured as a function of angle. The samples were cut into cantilevers (12 mm×2 mm) with a long axis at different angles, ϑ, from Si[110]. The substrate bending due to the magnetostrictive strain was measured relative to the pure Fe samples which were used to calibrate the instrument.

The measurements were fitted with the calculated angular dependence of the magnetostriction, summarized briefly here. The magnetostrictive strain in a cubic material along the direction β_1, β_2, β_3 when the crystal is magnetized along α_1, α_2, α_3 is given by

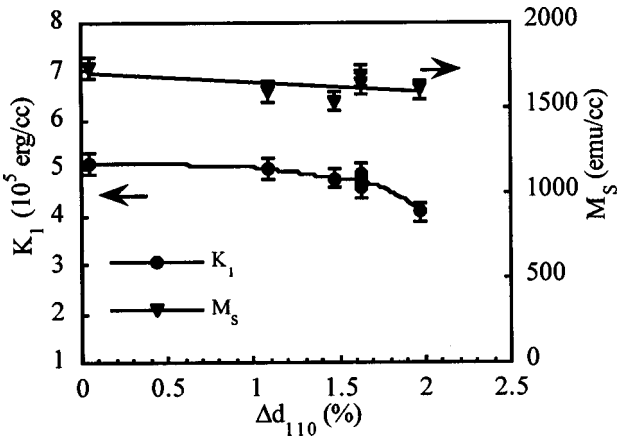

FIG. 17. Magnetocrystalline anisotropy constant, K_1 and saturation magnetization, M_S as a function of the normalized lattice dilation.

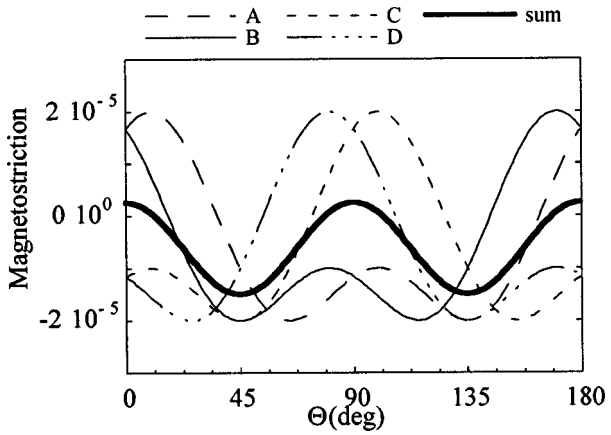

FIG. 18. Calculated magnetostriction of the four in-plane variants assuming that the strain is measured along the direction of the magnetization.

$$\frac{\delta l}{l}=\tfrac{3}{2}\lambda_{100}(\alpha_1^2\beta_1^2+\alpha_2^2\beta_2^2+\alpha_3^2\beta_3^2-\tfrac{1}{3}) +3\lambda_{111}(\alpha_1\alpha_2\beta_1\beta_2+\alpha_2\alpha_3\beta_2\beta_3+\alpha_3\alpha_1\beta_3\beta_1). \tag{9}$$

Assuming uniform stress the average magnetostrictive strain of the four variants can be calculated as

$$\frac{\delta l}{l}=\frac{1}{4}\left[\left(\frac{\delta l}{l}\right)_A+\left(\frac{\delta l}{l}\right)_B+\left(\frac{\delta l}{l}\right)_C+\left(\frac{\delta l}{l}\right)_D\right]. \tag{10}$$

Substituting the proper direction cosines for the four variants and assuming the strain is measured along the direction of the magnetization we can calculate the magnetostriction in the sample plane along an arbitrary direction at an angle θ degree from Si[110] as

$$\lambda=\frac{\delta l}{l}=(\tfrac{9}{32}[\lambda_{100}-\lambda_{111}]\cos 4\delta)\cos 4\theta +(\tfrac{11}{32}\lambda_{100}+\tfrac{21}{32}\lambda_{111}). \tag{11}$$

The calculated magnetostriction of the mosaic structure also has a fourfold symmetry (Fig. 18).

In the cantilever measurement system the maximum deflection of the cantilever is measured as the magnetization rotates in the plane of the cantilever.[40] Therefore the direction cosines of M_S and $\delta l/l$ in Eq. (9) are different. The deflection of the cantilever is proportional to the magnetostriction along the length of the cantilever, which can be obtained by substituting the direction cosines of the strain and the magnetization

$$\lambda(\vartheta,\theta)=\sqrt{q_1^2+q_2^2+2q_1q_2\cos 4\vartheta}\,\cos(2\theta+\varphi)+q_3, \tag{12}$$

where ϑ is the direction of the cantilever, θ is the angle of the magnetization in the sample plane; both are measured from the Si[110]. The q_1, q_2, q_3, and φ are simple combinations of λ_{100} and λ_{111}

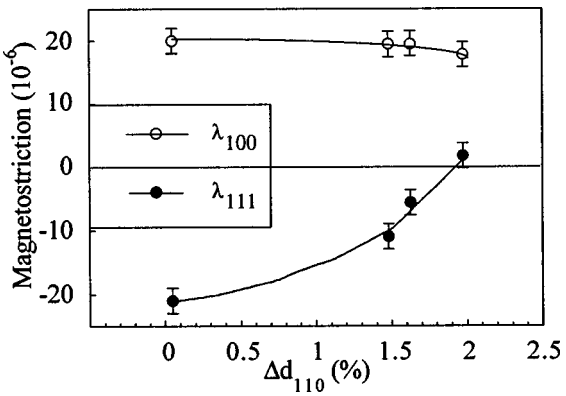

FIG. 19. Magnetostriction constants, λ_{100} and λ_{111}, as a function of lattice dilation.

$$q_1=\tfrac{9}{32}\lambda_{100}+\tfrac{15}{32}\lambda_{111}$$
$$q_2=\frac{9(\lambda_{100}-\lambda_{111})}{32}\cdot\cos 4\delta \tag{13}$$
$$q_3=\tfrac{2}{32}\lambda_{100}+\tfrac{6}{32}\lambda_{111}$$
$$\varphi=\vartheta-(1/2)\arctan[\Gamma\tan 2\vartheta]\ \text{ with }\ \Gamma=\pm\frac{q_1\pm q_2}{q_1\mp q_2}.$$

The constant Γ in φ, relation (13), depends on q_1 and q_2 and can be positive or negative depending on the signs and magnitudes of λ_{100} and λ_{111}. Because of the lock-in-detection technique used, the amplitude of the $\cos(2\theta+\varphi)$ term and φ in Eq. (12) were measured as a function of ϑ. By fitting Eq. (12) to the measured values of magnetostriction, the values of λ_{100} and λ_{111} were obtained as a function of lattice dilation (Fig. 19). It can be seen that λ_{100} only decreases slightly with nitrogen addition, whereas λ_{111} increased, and actually changes sign at ~2% lattice dilation. This measured behavior of λ_{100} and λ_{111} of FeTaN is the exact opposite of other researchers' theoretical predictions,[9,10] where λ_{100} was expected to increase linearly with increasing nitrogen content and λ_{111} to remain constant. At this point we cannot offer an explanation for the discrepancy between experiment and theory.

D. Comparison with results on (001) oriented epitaxial FeTaN films

It is worthwhile to compare the results for (110) films (10 wt% Ta) with those reported earlier on (001) films (5 wt% Ta). The deposition temperature was 200 °C for the (001) oriented films on MgO, and the (110) oriented samples were grown at ambient temperature, but the growth rates were approximately the same. The structural analysis showed that a secondary (221) twin orientation is present in the (001) oriented films at high nitrogen contents, while the (110) oriented films contained four in-plane variants of the same orientations, along with a secondary orientation of near (123), as was mentioned earlier. The secondary orientations were not included in the fitting of the crystalline anisotropy and magnetostriction measurements, since their amount was considered negligible based on the pole figure and TEM analysis. It was found in both cases that the magnetocrystal-

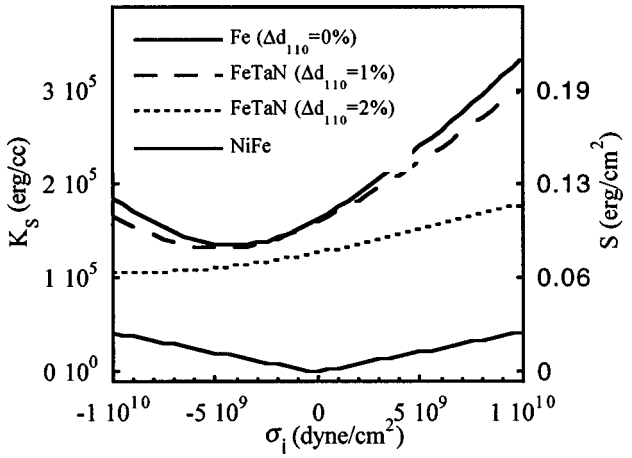

FIG. 20. Calculated local average anisotropy energy for FeTaN with different lattice dilations as a function of stress, and calculated structure or ripple constant, S assuming a thickness of 2000 Å and equiaxed grain size of 200 Å. The same curve is shown for $Ni_{81}Fe_{19}$ for comparison (lowest curve).

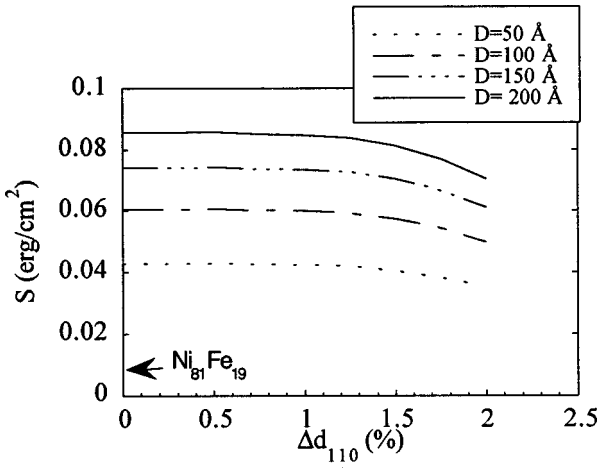

FIG. 21. Calculated structure constant of FeTaN as a function of lattice dilation for different equiaxed grain sizes assuming 2000 Å film thickness.

line anisotropy decreased with nitrogen addition, although the change was larger for the (001) than for the (110) oriented films, nevertheless the crystalline anisotropies remained in the same order (10^5 erg/cc) as of Fe. The magnitudes of the magnetostriction constants decreased for both the (001) and (110) orientations, but the sign change in λ_{111} was not observed in the (001) oriented samples.

One possible explanation for the differences in the measured constants in the two orientations is the underestimation of the secondary orientation in the (001) oriented films. However, approximately 30%–40% volume fraction of the (221) orientation combined with the principle (001) orientation would be required to explain the change in K_1 and magnetostriction constants of the films on MgO, compared to the (110) oriented films on Cu/Si. This is not justified by the structural analysis. It can be argued that the comparison of the results on the two orientations has no meaning, considering the differences in orientation, in Ta content, and in the bct deformation of the (001) and (110) films. This discrepancy is not unique in iron nitrides: measurements of (001) and (110) oriented $Fe_{16}N_2$ films grown by molecular beam epitaxy (MBE)[41] showed completely different magnetic properties in the two orientations, regarding the magnitude and sign of the anisotropy constants.

IV. RELATIONSHIP BETWEEN EPITAXIAL AND NANOCRYSTALLINE PROPERTIES

From the measured values of K_1, λ_{100}, and λ_{111}, we can calculate the average magnetic properties expected for nanocrystalline samples. The average local anisotropy, K_S, calculated from the measured fundamental constants as a function of isotropic thin film stress is shown in Fig. 20. It can be seen that the change in K_S with lattice dilation at the optimum stress values is relatively small. Also, substituting typical thickness (2000 Å) and grain size (200 Å) values for nanocrystalline FeTaN samples into Eq. (1), S can be calculated (Fig. 20). The values for permalloy are also plotted for comparison, assuming the same thickness and grain diameter as for the FeTaN films. The large difference in the minimum values of K_S for FeTaN and for NiFe is due to the large difference in K_1. The ripple parameter can also be plotted for different grain sizes as a function of nitrogen content for a typical thin film stress (-4×10^9 dyn/cm^2) (Fig. 21). The influence of the grain size and the stress is much more pronounced than the effect of the change in the fundamental constants with lattice dilation.

The saturation magnetostriction of nanocrystalline samples can also be predicted, since the values of λ_{100} and λ_{111} are known. The λ_S for $\langle 110\rangle$ fiber texture[9] assuming uniform stress in the averaging process (which is quite reasonable for Fe alloys[9]) is given as

$$\lambda_S^{\langle 110\rangle} = \tfrac{11}{32}\lambda_{100} + \tfrac{21}{32}\lambda_{111}. \tag{14}$$

The calculated value of λ_S using the measured values of λ_{100} and λ_{111} as a function of lattice dilation are in good agreement with published data[8] on nanocrystalline films with the same composition (Fig. 22) without any further assumptions about grain boundary materials. It is interesting to note that

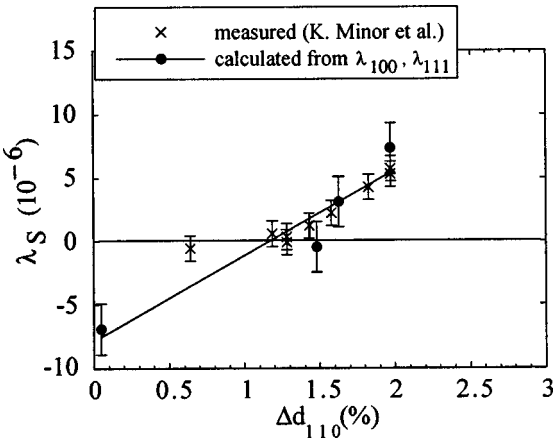

FIG. 22. Comparison of saturation magnetostriction calculated for nanocrystalline sample using the measured single crystal constant with the measured values for nanocrystalline sample (see Ref. 8) (courtesy of K. Minor and J. A. Barnard).

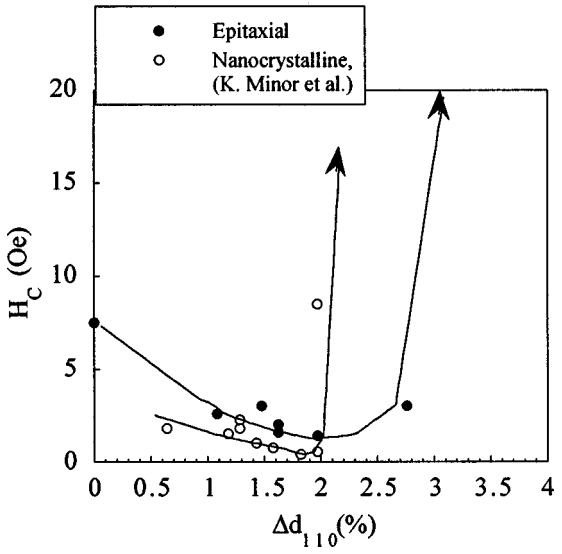

FIG. 23. Comparison of coercivities measured on nanocrystalline (see Ref. 42) and epitaxial FeTaN (10 wt% Ta) samples as a function of lattice dilation (courtesy of K. Minor and J. A. Barnard).

the smallest coercivity for both the epitaxial and polycrystalline films[42] occurs at the vicinity of 2% lattice dilation (Fig. 23).

One might argue that it is natural to arrive at a good agreement on calculated and measured average properties, because the measurement on epitaxial films gave average properties itself—averaged over four orientations—instead of direct measurement of the fundamental constants. Our strong argument in response is that the approach and analysis worked very well for the Fe films showing similar structural properties as the FeTaN films. We obtained the correct values for the fourth order crystalline anisotropy constant and for the ratio of the magnetostriction constants in the case of iron.

V. CONCLUSION

This research has focused on the fundamental magnetic and structural properties of epitaxial FeTaN alloy, in order to understand the governing forces of soft magnetism in its nanocrystalline phase.

We successfully optimized deposition conditions for the epitaxial growth of Fe and FeTaN thin films on Cu(001)/Si(001) single crystal substrates using dc magnetron sputtering. The growth of Fe was in agreement with earlier reports, while no investigation on the epitaxial growth of FeTaN has been carried out so far.

On the basis of the structural characterization used to interpret the magnetic measurements, the magnetocrystalline anisotropy and the magnetostriction constants of Fe were, in fact, influenced by the tantalum and nitrogen additions. The observed values of the magnetostriction constants contradicted the earlier theoretical predictions. This fact questions the range of applicability of the model and urges rethinking the role of interstitials in thin films of Fe alloys. Furthermore, the average saturation magnetostriction, calculated from the measured values of λ_{100} and λ_{111}, showed a linear increase with nitrogen addition in a comforting agreement with the experimental results of others on nanocrystalline films.

The central parameter of the ripple theory was determined for the alloy using the measured fundamental constants of epitaxial films, and it was found that soft magnetism is not achieved through the reduction of the local anisotropy energy, but through other structural means. This is in agreement with earlier findings on the nanocrystalline state of the material. Moreover, it implies, that unless the structural properties are fully optimized, the magnetic dispersions will be intrinsically more significant than that of permalloy.

ACKNOWLEDGMENTS

The authors thank J. A. Barnard and K. Minor for many helpful discussions and providing the raw data of their published results on nanocrystalline FeTaN films. They also thank T. Kuiper of Philips Research Laboratories for the Auger and RBS measurements. This project was partially supported by the MRSEC Program of the National Science Foundation under Award No. DMR-9400399, and by a grant from the U.S. Department of Commerce administered by NSIC, and by the Assistant Secretary for Energy Efficiency and Renewable Energy, Office of Transportation Technologies, as part of the High Temperature Materials Laboratory User Program, Oak Ridge National Laboratory, managed by Lockheed Martin Energy Research Corp. for the U.S. Department of Energy under Contract No. DE-AC05-96OR22464.

[1] C. D. Mee and E. D. Daniel, in *Magnetic Recording Technology* (McGraw–Hill, New York, 1996), Sec. 6.1.
[2] O. Kohmoto, IEEE Trans. Magn. **27**, 3640 (1991).
[3] B. Viala, M. K. Minor, and J. A. Barnard, J. Appl. Phys. **80**, 3941 (1996).
[4] N. Robertson, H. L. Hu, and C. Tsang, IEEE Trans. Magn. **33**, 2818 (1997).
[5] G. Qiu, E. Haftek, and J. A. Barnard, J. Appl. Phys. **73**, 6573 (1993).
[6] E. Haftek and J. A. Barnard, IEEE Trans. Magn. **30**, 3915 (1994).
[7] V. R. Inturi and J. A. Barnard, IEEE Trans. Magn. **31**, 2660 (1995).
[8] M. K. Minor, B. Viala, and J. A. Barnard, IEEE Trans. Magn. **31**, 5005 (1995).
[9] J. C. Cates and C. Alexander, J. Appl. Phys. **75**, 6754 (1994).
[10] G. De Vries, Physica (Amsterdam) **25**, 1211 (1959).
[11] H. Hoffmann, IEEE Trans. Magn. **4**, 32 (1968).
[12] H. Hoffmann, Phys. Status Solidi **33**, 175 (1969).
[13] H. Hoffmann, Thin Solid Films **58**, 223 (1979).
[14] K. Kempter and H. Hoffmann, Phys. Status Solidi **34**, 237 (1969).
[15] W. D. Doyle and T. F. Finnegan, J. Appl. Phys. **39**, 3355 (1968).
[16] E. Haftek, L. Varga, W. D. Doyle, and J. A. Barnard, IEEE Trans. Magn. **31**, 3973 (1995).
[17] S. Chikazumi, in *Physics of Magnetism* (Wiley, New York, 1964), pp. 130, 173.
[18] M. Takahashi and T. Shimatsu, IEEE Trans. Magn. **26**, 1485 (1990).
[19] J. C. Cates, Ph.D. thesis, University of Alabama, 1993.
[20] *Binary Alloy Phase Diagrams*, edited by T. B. Massalski (Metals Park, OH, 1986), Vol. 1.
[21] B. Hoekstra, E. M. Gyorgy, G. Zydzik, and P. J. Flanders, Rev. Sci. Instrum. **48**, 1253 (1977).
[22] J. F. Freedman, IBM J. Res. Dev. **6**, 449 (1962).
[23] L. Varga and W. D. Doyle, J. Appl. Phys. **79**, 4995 (1996).
[24] L. Varga, W. D. Doyle, T. Klemmer, P. J. Flanders, and K. J. Kozaczek, IEEE Trans. Magn. **32**, 3542 (1996).
[25] L. Varga, A. Stephenson, S. Timkovich, T. Klemmer, W. D. Doyle, and K. J. Kozaczek, IEEE Trans. Magn. **33**, 3616 (1997).
[26] M. Kato, M. Wada, A. Sato, and T. Mori, Acta Metall. **37**, 749 (1989).

[27] B. G. Demczyk, V. M. Naik, A. Lukaszew, R. Naik, and G. W. Auner, J. Appl. Phys. **80**, 5035 (1996).
[28] C. Chang, J. C. Liu, and J. Angilello, Appl. Phys. Lett. **57**, 2239 (1990).
[29] B. G. Demczyk, R. Naik, G. Auner, C. Kota, and U. Rao, J. Appl. Phys. **75**, 1956 (1994).
[30] V. A. Burrows, Y. J. Chabat, G. S. Higashi, K. Raghavachari, and S. B. Christman, Appl. Phys. Lett. **53**, 998 (1988).
[31] E. P. Brahamson and S. L. Lopata, AIME TRANS. **236**, 76 (1966).
[32] R. E. Reed-Hill, *Physical Metallurgy Principles*, 3rd. (PWS-Kent, Boston, 1992).
[33] H. A. Wriedt, N. A. Gocken, and R. H. Nafziger, Bull. Alloy Phase Diagrams **8**, (1987).
[34] C. Laird, E. Eichen, and W. R. Bitler, J. Appl. Phys. **37**, 2225 (1966).
[35] U. Dahmen and K. H. Westmacott, Mater. Res. Soc. Symp. Proc. **229**, 167 (1991).
[36] P. H. Pumphrey and K. M. Bowkett, Scr. Metall. **5**, 365 (1971).
[37] D. G. Brandon, Acta Metall. **14**, 1479 (1966).
[38] R. Naik, C. Kota, J. S. Payson, and G. L. Dunifer, Phys. Rev. B **48**, 1008 (1993).
[39] A. Tam and Schroeder, IEEE Trans. Magn. **25**, 2629 (1989).
[40] L. Varga, H. Jiang, T. Klemmer, and W. D. Doyle, IEEE Trans. Magn. (in press).
[41] Y. Sugita, K. Mitsuoka, M. Komuro, H. Hoshiya, Y. Kozono, and M. Hanazono, J. Appl. Phys. **70**, 5977 (1991).
[42] K. Minor, M. S. thesis, University of Alabama, 1997.